Voltage-Controlled Magnetic Anisotropy in Heterostructures with Atomically Thin Heavy Metals

Sohee Kwon,[1,][*] Qilong Sun,[1] Farzad Mahfouzi,[1] Kang L. Wang,[2] Pedram Khalili Amiri,[3] and Nicholas Kioussis[1,][†]

[1]*Department of Physics and Astronomy, California State University, Northridge, California 91330-8268, USA*

[2]*Department of Electrical and Computer Engineering, University of California, Los Angeles, Los Angeles, California 90095-1594, USA*

[3]*Electrical Engineering and Computer Science, Northwestern University, Evanston, Illinois 60208-3109, USA*

The demand for higher-density, higher-speed, and more energy-efficient magnetoelectric RAM (MeRAM) requires the search of promising materials and magnetic-tunnel-junction stacks with voltage-controlled magnetic anisotropy (VCMA) efficiency greater than the 1000 fJ/(Vm). Using first-principles electronic structure calculations, we propose a double-barrier ferromagnetic heterostructure with an atomically thin *late* transition metal X (Rh, Ir, Pt), which exhibits *both* giant perpendicular magnetic anisotropy (PMA) and VCMA efficiency, where the former (latter) is 1 (1 to 2) order of magnitude higher than the values reported to date. We demonstrate that the dominant contribution to both the PMA and VCMA arises from the late heavy metal X due to the large biaxial tensile strain-induced magnetism in X. Furthermore, we predict a sign reversal of the VCMA efficiency from the Ir- to the Pt-monolayer cap. We elucidate that the underlying mechanism is the electric-field-induced energy shift of the spin-polarized d_{z^2}-derived projected states on the X layer. These findings provide useful guiding rules in exploiting the large spin-orbit coupling and biaxial tensile strain-induced magnetism in the late $5d$-transition metals for the design of the next generation of ultra-low energy MeRAM devices.

I. INTRODUCTION

Magnetic RAM (MRAM) devices based on current-induced switching schemes, such as spin-transfer torque (STT) or spin-orbit torque (SOT), are promising candidates for faster and more energy-efficient memory units in the next-generation integrated electronic systems [1–4]. Despite the successful achievement of nonvolatile memory, one of the key challenges for MRAMs is the requirement of large dynamic switching energy and high current densities, which in turn results in Joule heating [5]. On the other hand, magnetoelectric RAM (MeRAM) using the voltage-controlled magnetic anisotropy (VCMA) mechanism has attracted considerable attention recently as an alternative route to control and manipulate the magnetization in low-power and fast-switching magnetic tunnel junctions (MTJs) [6]. MeRAM provides similar density as dynamic RAM (DRAM) and lower switching energy per bit (approximately 1–6 fJ) than STT RAM. In addition, MeRAM has the fastest speed (approximately 1–5 ns) to write and read information among all RAM technologies [7–9].

The electric-field-induced change of the magnetocrystalline anisotropy (MCA) energy of a MTJ stack (in the linear-bias regime) is $\Delta(\text{MCA}) = E_{\text{MCA}}(E_{ext}) - E_{\text{MCA}}(0) = \beta E_I = \beta E_{\text{ext}}/\epsilon_\perp$. Here, E_I is electric field in the insulator, β is the VCMA coefficient, and $\epsilon_\perp$ is the out-of-plane component of the relative dielectric constant tensor of the insulator, which depends on the strain and the type of insulator [10,11]. MeRAM devices with switching energies down to 6 fJ/bit and subnanosecond switching speeds have been demonstrated experimentally [7,12]. A wide range of values for both the MCA (0.5–2.3 erg/cm^2) [13–17] and VCMA efficiency (20–1000 fJ/Vm) [13,18–20] has been experimentally reported. These depend on various factors, such as the seed or cap material adjacent to the ferromagnet-barrier stack, doping layers at the ferromagnet-barrier interface, insertion layers in the ferromagnet-free layer, epitaxial or sputter growth, etc. (see Fig. 4 in Ref. [13]). On the theoretical side, two different underlying mechanisms have been proposed. The first one is the voltage-induced modification of the electron occupancy of d orbitals of different symmetries at the interfacial magnetic layer, which in turn yield different contributions to the MCA [21–23]. The second one is the voltage-induced shifts of pairs of occupied and unoccupied d-derived bands of interfacial magnetic layers

[*]sohee.kwon.866@my.csun.edu

[†]nick.kioussis@csun.edu

with different symmetries, which are coupled via the out-of or in-plane components of the orbital angular-momentum operator $\vec{L}$ [10,11,24–26].

The demand for higher-density, higher-speed, and lower-energy MeRAM faces two grand challenges [13,27]. The first one, the so-called "1000 challenge," requires a VCMA efficiency >1000 fJ/(Vm). The second one requires a perpendicular magnetic anisotropy (PMA) higher than 2 erg/cm². The VCMA coefficient is inversely proportional to the cross-sectional area of the MTJ and the higher its value, the lower the voltage and energy needed to switch the magnetic state. Thus, there is an urgent need to search and identify new materials and MTJ architectures that have higher PMA and VCMA efficiencies.

Using *ab initio* electronic structure calculations, we predict that double-barrier MgO/X/FeCo/MgO heterostructure with an atomically thin insertion $X = $ Ir, Pt, Rh layer between the FeCo and MgO exhibits both *giant* PMA and VCMA efficiency values where the former (latter) is 1 (1 to 2) order of magnitude higher than the values reported to date. The underlying atomic mechanism lies on the synergy of three crucial effects: (1) the emergence of magnetism on the X layer is mainly due to the biaxial tensile strain (in addition to the proximity-induced magnetic effect), which occurs in the late-transition heavy metals; (2) the large spin-orbit coupling (SOC) of the heavy metal X (approximately equal to 0.5 eV), which provide the most dominant (approximately equal to 90%) contribution to the total PMA; and (3) the electric field in the MgO next to the *ferromagnetic* heavy metal provides a *giant* modulation of the PMA of X resulting in record-high VCMA values [17 000 fJ/(Vm)].

II. METHODOLOGY

The first-principles electronic structure calculations are carried out within the projector augmented-wave method [28], as implemented in the Vienna *ab initio* simulation package (VASP) [29]. The generalized gradient approximation is used to describe the exchange-correlation functional as parametrized by Perdew, Burke, and Ernzerhof (PBE) [30]. The slab supercell for the MgO/X/FeCo/MgO (001) junction along [001], shown in Fig. 2(d), consists of a single monolayer (ML) of fcc X on top of three MLs of B2-type FeCo sandwiched between two five MLs of rocksalt MgO films and a 15-Å-thick vacuum region. The O atoms at the FeCo/MgO interface are placed atop the Fe atoms, which is the most stable configuration [22,24,25]. We denote with Fe_1 and Fe_2 the atoms at the Fe/MgO and Fe/X interfaces, respectively. The in-plane lattice constant is set equal to the theoretical lattice constant of bulk FeCo of 2.84 Å and the relative dielectric constant of MgO for this lattice constant (MgO is under a biaxial compressive strain of approximately equal to -4%) is $\varepsilon_\perp/\varepsilon_0 = 27$ [10]. We use an energy cutoff of 500 eV

and a $16 \times 16 \times 1$ k-point mesh to relax the z components of the atomic coordinates for each electric field until the largest force becomes less 5×10^{-3} eV/Å and the change in the total energy between two ionic relaxation steps is smaller than 10^{-6} eV. The dipole corrections are taken into account along the [001] direction. The SOC of the valence electrons is in turn included using the second-variation method [31] employing the scalar-relativistic eigenfunctions of the valence states and a $32 \times 32 \times 1$ k-point mesh. The MCA per unit interfacial area, A, is determined from $(E_{[100]} - E_{[001]})/A$, where $E_{[100]}$ and $E_{[001]}$ are the total energies with magnetization along the [100] and [001] directions, respectively.

III. RESULTS AND DISCUSSION

A ubiquitous and crucial feature of the heavy metal (HM)-ferromagnet (FM) interface is the epitaxial strain, which can have a dramatic effect on the emergence of magnetism on the HM, which, however, is not associated with the well-known proximity effect (induced magnetic moment on the HM via the proximity of the FM). More specifically, on going from the early (Ta, W) to late (Ir, Pt, Au) transition metals across the 5d series there is a change of stable crystal structure from bcc to hcp to fcc. More importantly, the early (late) thin HM films are under giant (few %) biaxial *compressive (tensile)* strain relative to the FeCo, which can in turn modulate the magnetic properties of the HM.

In order to study the effect of strain we carry out total-energy calculations of homogenous magnetic spin spirals for a freestanding X ($X = $ Pt, Rh, and Ir) monolayer using the generalized Bloch theorem within the scalar-relativistic approach [32]. For the range of strain ($\pm6\%$) we find that the total energy, $E(\mathbf{q})$, of planar spiral ($\mathbf{q}$ is the wave-vector propagation of the spin spiral) is minimum for $\mathbf{q} = 0$, indicating that the ground state is ferromagnetic. This result is in agreement with previous electronic structure calculations [33,34]. The variation of the magnetic moment per atom for the freestanding FM monolayer is plotted versus the biaxial strain, $\eta = (a - a_o)/a_o$, in Fig. 1, where a_o is the equilibrium lattice constant of bulk X. Under a wide range of biaxial tensile strain (vertical arrows denote the strain imposed by the FeCo on X) the Ir, Rh, and Pt freestanding MLs have magnetic moments of about 1.69, 1.55, and 0.67 μ_B, respectively. Previous *ab initio* calculations have also reported the emergence of magnetism in freestanding late 5d-transition metal monolayers [33] and late 5d/X (001) ($X = $ Ag, Au) bilayers [34]. However, these calculations did not investigate the effect of strain and/or electric field on magnetism. The underlying origin of the emergence of magnetism lies on (i) the increase of localization of the d-wave functions and the concomitant narrowing of the 5d bandwidth moving to the late transition metals, and (ii) the raise of the local density
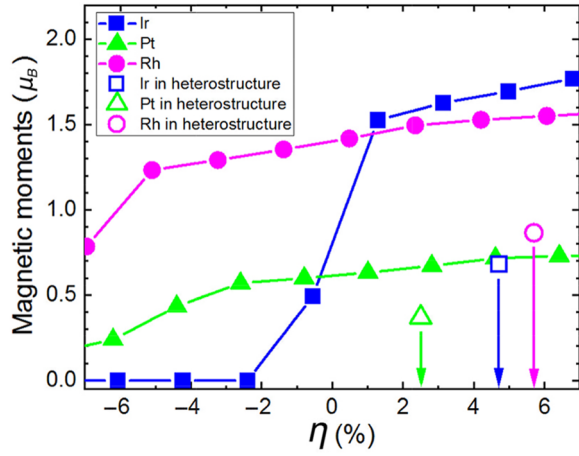
FIG. 1. Magnetic moment per atom of freestanding X, ($X =$ Ir, Pt, and Rh) monolayer (closed squares, triangles, and circles for Ir, Pt, and Rh, respectively) versus biaxial strain on X, $\eta = (a - a_o)/a_o$, where a_o is the equilibrium lattice constant of bulk X. The open squares, triangles, and circles denote the magnetic moments of the X monolayer in the MgO/X/FeCo/MgO heterostructure under the biaxial tensile strain (indicated by the vertical arrows) imparted by the FeCo on the atomically thin X layer.

FIG. 2. Magnetic anisotropy of the proposed MgO(5)/X(1)/FeCo(3)/MgO(5) (001) stack architecture as a function of electric field in MgO for $X =$ (a) Ir, (b) Pt, and (c) Rh, where the numbers in the parentheses denote the number of MLs. (d) Schematic atomic structure where the Fe_1 and Fe_2 denote iron atoms adjacent to the MgO and X layer, respectively. The arrow along [001] indicates the positive direction of the external electric field.

of states (DOS) of the antibonding states associated with the two-dimensional band structure [34]. Note that the X atom moments in the MgO/X/FeCo/MgO heterostructure (open symbols) are reduced by about a factor of 2 compared to the values in the freestanding ML under the same tensile strain due to the hybridization of the X/5d–Fe/3d orbitals [33].

Having established the emergence of strain-induced magnetism in the atomically thin X layer we next investigate its role on both the PMA and VCMA in the MgO(5)/X(1)/FeCo(3)/MgO(5) heterostructure, which can be grown experimentally using atomic-layer-deposition (ALD) or pulsed-layer-deposition (PLD) techniques [35]. Figure 2 shows the variation of the MCA energy as a function of electric field in the insulator for (a) Ir, (b) Pt, and (c) Rh, respectively. First, we find very large zero-field PMA values of 14.7, 4.8, and 3.9 erg/cm^2 for Ir, Pt, and Rh, respectively, compared to the range of 0.7–2.2 erg/cm^2 values often reported in experiments [13] for different HM caps and growth conditions. Second, and more importantly, we predict *giant* VCMA coefficients, $|\beta|$, of 17 000, 5886, and 313 fJ/(Vm) for Ir, Pt, and Rh, respectively, compared to the range of about 20–400 fJ/(Vm) of most experimentally reported values [13]. A significant enhancement of VCMA efficiency was also experimentally observed in Ir-doped FM-insulator MTJs [36]. However, our results suggest that epitaxial insertion of the heavy-metal atomic layers at the Fe/MgO might enhance the VCMA even further. This is in agreement with the previous theoretical prediction of large VCMA
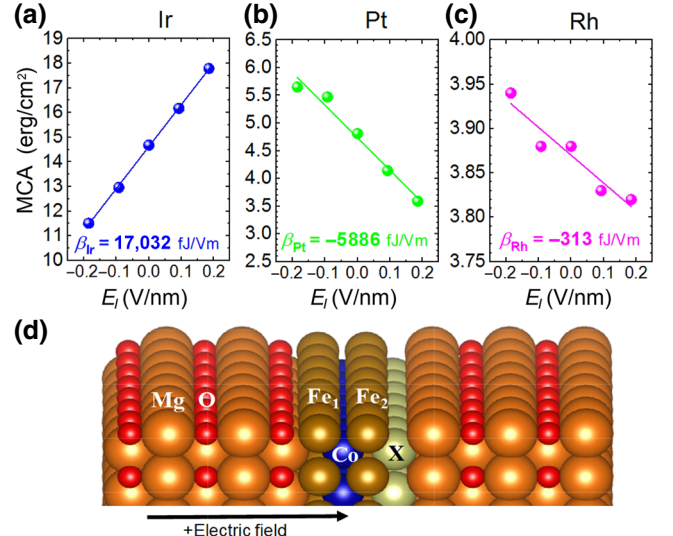
for Au/Fe/X/MgO heterostructure [25], where an in-plane MCA was observed in contrast to the large PMA predicted in our double barrier heterostructure. Third, there is a sign reversal of the VCMA efficiency from Ir to Pt. These results invite several intriguing questions on the origin in the electronic structure of the enhancement of both the PMA and VCMA efficiency including the sign reversal of β from Ir to Pt.

In order to understand the underlying mechanism of both the PMA and VCMA behavior, we calculate the difference in SOC energies between the in- ($\parallel$) and out-of-plane ($\perp$) magnetization orientation, $\Delta E_{\text{SOC}} = (E_{\text{SOC}}^{\parallel} - E_{\text{SOC}}^{\perp})/2$, where

$$E_{\text{SOC}} = \frac{\hbar^2}{2m^2c^2} \left\langle \frac{1}{r}\frac{dV}{dr}\vec{\hat{L}}\cdot\vec{\hat{S}} \right\rangle$$
$$= \sum_{I,lmm'\sigma\sigma'} \xi_{Il}\langle Ilm\sigma|\vec{\hat{L}}\cdot\vec{\hat{S}}|Ilm'\sigma'\rangle\rho_{mm',\sigma\sigma'}^{Il}. \quad (1)$$

Here,

$$\rho_{mm',\sigma\sigma'}^{Il} = \frac{1}{N_k}\sum_{nk}\langle Ilm'\sigma'|nk\rangle\langle nk|Ilm\sigma\rangle f(\varepsilon_{nk}), \quad (2)$$

I is the atomic index, lm are the angular-momentum orbitals, σ, σ' is the spin index, ξ_{Il} is the atomic SOC strength obtained from the spherical part of the effective

potential, $V(r)$, within the PAW sphere, $\rho_{mm',\sigma\sigma'}^{ll}$ is the density matrix projected on atomic orbitals, and $\vec{\hat{L}}$ and $\vec{\hat{S}}$ are the orbital and spin operators, respectively.

Figure 3 shows the total ΔE_{SOC} (red triangles) and MCA energy (black circles) for zero and ± 0.19 V/nm electric field in the insulator for (a) Ir, (b) Pt, and (c) Rh insertion, respectively. We also display the layer-projected, ΔE_{SOC}, on the interfacial Fe_1 and Fe_2 atoms adjacent to MgO and X systems, respectively, and the X atoms. These results reveal several points: first, the dominant contribution to the total ΔE_{SOC} for Ir and Pt arises from the X layer independent of the electric field. Second, the E-field dependence of the Fe-projected ΔE_{SOC} is weak in sharp contrast to the strong E-field dependence of the X-projected ΔE_{SOC}, which in turn determines the overall VCMA efficiency. Third, even though the MCA $\neq \Delta E_{SOC}$ for Ir and Pt layers for any field (failure of the perturbation theory due to the strong SOC of about 0.45 and 0.49 eV for Ir and Pt, respectively), the change of MCA or change of ΔE_{SOC} per unit of electric field (slope) are about the same. In contrast for Rh, which has a weaker SOC of 0.15 eV we find that $\Delta E_{SOC} \approx$ MCA (about 3% difference) [37]. Furthermore, both the Rh and Fe_1 atoms yield dominant contributions to both the PMA and VCMA for the Rh insertion. Overall, these results clearly demonstrate that both the PMA and VCMA efficiency in the MgO/X/FeCo/MgO stack architecture is controlled by the X layer, which is magnetic, has large SOC, and is adjacent to the insulator (where the electric field is present), giving rise to a giant E-field-induced change of MCA.

In order to elucidate the microscopic origin of the dominant contribution of the Ir or Pt ML to both the PMA and VCMA, we calculate the X/5d-orbital-projected
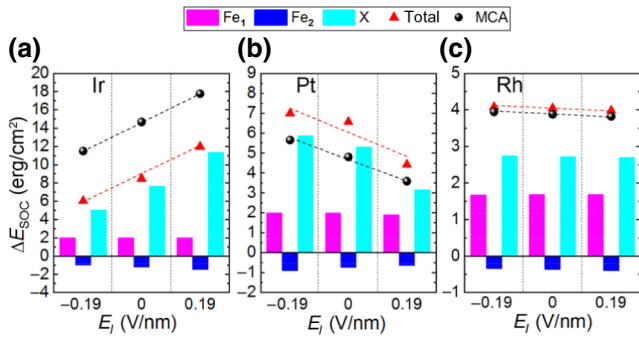

FIG. 3. Difference in total SOC energies between the in- ($\parallel$) and out-of-plane ($\perp$) magnetization orientation, ΔE_{SOC} (red triangles), and MCA energies (black circles) of the MgO/X/FeCo/MgO heterostructure under zero and ± 0.19 V/nm electric field in the insulator for $X =$ (a) Ir, (b) Pt, and (c) Rh, respectively. Bar graphs represent the atom-resolved ΔE_{SOC}, for the X (light blue) atoms and the interfacial Fe_1 (purple) and Fe_2 (dark blue) atoms adjacent to MgO and X, respectively.
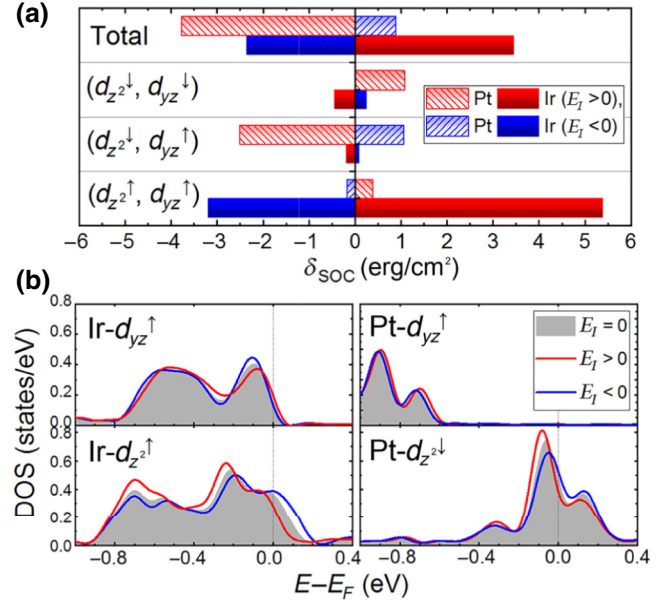

FIG. 4. (a) The $\langle d_{z^2}^\sigma | \hat{L}_x | d_{yz}^{\sigma'} \rangle$ contributions to the *E-field-induced change* of SOC energies, $\delta_{SOC} = \Delta E_{SOC}(\mathbf{E_I}) - \Delta E_{SOC}(\mathbf{E_I} = 0)$, for both Ir (solid bars) and Pt (hatched bars) under $+0.19$ V/nm (red) and -0.19 V/nm (blue), electric field in the insulator, respectively. We also show the total δ_{SOC}. (b) Atom (Ir or Pt) and spin-projected density of states of d_{z^2} and d_{yz} orbitals under zero (shaded area), $+0.19$ V/nm (red curves), and -0.19 V/nm (blue curves) E field, respectively.

contributions to the ΔE_{SOC}. For both Ir and Pt, we find that the *E-field-induced change* of SOC energies originates primarily from the SOC of the $d_{z^2}^\sigma$- and $d_{yz}^{\sigma'}$-derived states of X via the in-plane orbital angular-momentum operator, $\hat{L}_x$. Thus, in Fig. 4(a) we display the bar graph of the $\langle d_{z^2}^\sigma | \hat{L}_x | d_{yz}^{\sigma'} \rangle$ contributions to the *E-field-induced change* of SOC energies, $\delta_{SOC} = \Delta E_{SOC}(\mathbf{E_I}) - \Delta E_{SOC}(\mathbf{E_I} = 0)$, for both Ir and Pt under $+0.19$ V/nm (red) and -0.19 V/nm (blue). It is important to note that for Ir the $\langle d_{z^2}^\uparrow | \hat{L}_x | d_{yz}^\uparrow \rangle$ (spin-diagonal matrix elements) yields the dominant contribution to δ_{SOC}, which in turn increases (decreases) under positive (negative) electric field. In sharp contrast, the increase of band filling on going to Pt renders the $\langle d_{z^2}^\downarrow | \hat{L}_x | d_{yz}^\uparrow \rangle$ dominant, which, however, increases (decreases) under negative (positive) E field.

The sign reversal of the VCMA coefficient from Ir to Pt can be understood from the second-order perturbation theory expression for the MCA, given by Ref. [38]

$$E_{MCA} \approx \sum_{o,u,\sigma\sigma'} \sigma\sigma' \frac{|\langle \Psi_u^\sigma | \hat{\xi} \hat{L}_z | \Psi_o^{\sigma'} \rangle|^2 - |\langle \Psi_u^\sigma | \hat{\xi} \hat{L}_x | \Psi_o^{\sigma'} \rangle|^2}{E_u^\sigma - E_o^{\sigma'}}$$

$$\approx \sum_{I,lmm'\sigma\sigma'} \sum_{o,u} \sigma\sigma' \xi_{ll}^2 \frac{P_u^{Ilm\sigma} P_o^{Ilm'\sigma'}}{E_u^\sigma - E_o^{\sigma'}} \Delta L_{l,mm'}, \quad (3)$$

where

$$\Delta L_{l,mm'} = |\langle lm|\hat{L}_z|lm'\rangle|^2 - |\langle lm|\hat{L}_x|lm'\rangle|^2. \quad (4)$$

Here, $\sigma, \sigma' \equiv \pm 1$ denote the electron spin, $\hat{\xi}$ is a diagonal matrix containing the SOC strength, $\Psi_o^\sigma(E_o^\sigma)$ and $\Psi_u^\sigma(E_u^\sigma)$ are the one-electron occupied and unoccupied spin-polarized Bloch states (energies) of band index n and wave vector k (omitted for simplicity) and $\hat{L}_{x(z)}$ is the $x(z)$ component of the orbital angular-momentum operator, $P_n^{Ilm\sigma} = |\langle \Psi_n^\sigma \rangle Ilm|^2$ is the Bloch-wave amplitude projected on atom I (in our case X), orbital index lm, and spin index σ.

Similarly to the E-field-induced change of SOC energies, the electric field has a larger effect primarily on the $d_{z^2}^{\uparrow(\downarrow)}$- and $d_{yz}^\uparrow$-derived Ir (Pt) projected DOS (PDOS), which are shown in Fig. 4(b). Under positive (negative) E field the Ir-$d_{z^2}^\uparrow$- and Pt-$d_{z^2}^\downarrow$-derived DOS shift downward in energy, leading to the reduction (increase) of the number of unoccupied d_{z^2} states around the Fermi energy. We find that the electric-field-induced shift of the Ir-derived DOS is primarily due to the electric-field-induced charge accumulation, while the electric-field changes of atomic-position displacements have a moderate contribution. In contrast, there is a small effect on the $d_{yz}^\uparrow$-derived PDOS. In view of the (i) dominant contribution of the $\langle d_{z^2}^{\uparrow(\downarrow)}|\hat{L}_x|d_{yz}^\uparrow\rangle$ of Ir (Pt) to the MCA and (ii) the $(\sigma\sigma')$ prefactor in Eq. (3), the reduction of unoccupied $d_{z^2}^{\uparrow(\downarrow)}$ PDOS near the Fermi energy under positive E field results in the increase (decrease) of the MCA in the Ir (Pt) overlayer, consistent with the positive (negative) VCMA coefficient in Fig. 3.

IV. CONCLUSION

In summary, we predict that the MgO/X/FeCo/MgO heterostructure, where X is an atomically thin *late* transition metal (Ir, Pt, Rh), exhibits *both* giant perpendicular magnetic anisotropy (PMA) and VCMA efficiency. These primarily arise from the X insertion, which has large SOC and becomes magnetic under biaxial tensile strain. The underlying mechanism for the ultra-high VCMA efficiency is the SOC of the $d_{z^2}^\sigma$- and $d_{yz}^{\sigma'}$-derived states of X via the in-plane orbital angular momentum. These theoretical findings serve as simple guiding rules for future experimental design of higher-speed and more energy-efficient magnetoelectric devices employing controlled fabrication of ultra-thin transition metal insertions under appropriate biaxial tensile strain growth conditions [20].

[1] J. C. Slonczewski, Current-driven excitation of magnetic multilayers, J. Magn. Magn. Mater. **159**, L1 (1996).

[2] L. Berger, Emission of spin waves by a magnetic multilayer traversed by a current, Phys. Rev. B **54**, 9353 (1996).

[3] F. Mahfouzi and N. Kioussis, First-principles study of the angular dependence of the spin-orbit torque in Pt/Co and Pd/Co bilayers, Phys. Rev. B **97**, 224426 (2018).

[4] I. M. Miron, G. Gaudin, S. Auffret, B. Rodmacq, A. Schuhl, St. Pizzini, J. Vogel, and P. Gambardella, Current-driven spin torque induced by the Rashba effect in a ferromagnetic metal layer, Nat. Mater. **9**, 230 (2010).

[5] C. Chappert, A. Fert, and F. N. Van Dau, The emergence of spin electronics in data storage, Nat. Mater. **6**, 813 (2007).

[6] Y. Shiota, T. Nozaki, F. Bonell, S. Murakami, T. Shinjo, and Y. Suzuki, Induction of coherent magnetization switching in a few atomic layers of FeCo using voltage pulses, Nat. Mater. **11**, 39 (2012).

[7] C. Grezes, F. Ebrahimi, J. G. Alzate, X. Cai, J. A. Katine, J. Langer, B. Ocker, P. K. Amiri, and K. L. Wang, Ultra-low switching energy and scaling in electric-field-controlled nanoscale magnetic tunnel junctions with high resistance-area product, Appl. Phys. Lett. **108**, 012403 (2016).

[8] Y. Shiota, T. Nozaki, S. Tamaru, K. Yakushiji, H. Kubota, A. Fukushima, S. Yuasa, and Y. Suzuki, Reduction in write error rate of voltage-driven dynamic magnetization switching by improving thermal stability factor, Appl. Phys. Lett. **111**, 022408 (2017).

[9] R. Dorrance, J. G. Alzate, S. S. Cherepov, P. Upadhyaya, I. N. Krivorotov, J. A. Katine, J. Langer, K. L. Wang, P. K. Amiri, and D. Markovic, Diode-MTJ crossbar memory cell using voltage-induced unipolar switching for high-density MRAM, IEEE Electron Device Lett. **34**, 753 (2013).

[10] P. V. Ong, N. Kioussis, D. Odkhuu, P. K. Amiri, K. L. Wang, and G. P. Carman, Giant voltage modulation of magnetic anisotropy in strained heavy metal/magnet/insulator heterostructures, Phys. Rev. B **92**, 020407(R) (2015).

[11] P. V. Ong, N. Kioussis, P. K. Amiri, and K. L. Wang, Electric-field-driven magnetization switching and nonlinear magnetoelasticity in Au/FeCo/MgO heterostructures, Sci. Rep. **6**, 29815 (2016).

[12] S. Kanai, F. Matsukura, and H. Ohno, Electric-field-induced magnetization switching in CoFeB/MgO magnetic tunnel junctions with high junction resistance, Appl. Phys. Lett. **108**, 192406 (2016).

[13] X. Li, A. Lee, S. A. Razavi, H. Wu, and K. L. Wang, Voltage-controlled magnetoelectric memory and logic devices, MRS Bull. **43**, 970 (2018). and references therein.

[14] F. Matsukura, Y. Tokura, and H. Ohno, Control of magnetism by electric fields, Nat. Nanotechnol. **10**, 209 (2015).

[15] T. Liu, J. W. Cai, and L. Sun, Large enhanced perpendicular magnetic anisotropy in CoFeB/MgO system with the typical Ta buffer replaced by an Hf layer, AIP Adv. **2**, 032151 (2012).

[16] C. Pai, M. Nguyen, C. Belvin, L. H. Vilela-Leao, D. C. Ralph, and R. A. Buhrman, Enhancement of perpendicular magnetic anisotropy and transmission of spin-Hall-effect-induced spin currents by a Hf spacer layer in W/Hf/CoFeB/MgO layer structures, Appl. Phys. Lett. **104**, 082407 (2014).

[17] D. C. Worledge, G. Hu, D. W. Abraham, J. Z. Sun, P. L. Trouilloud, J. Nowak, S. Brown, M. C. Gaidis, E. J. O'Sullivan, and R. P. Robertazzi, Spin torque switching of perpendicular Ta—CoFeB—MgO-based magnetic tunnel junctions, Appl. Phys. Lett. **98**, 022501 (2011).

[18] M. Endo, S. Kanai, S. Ikeda, F. Matsukura, and H. Ohno, Electric-field effects on thickness dependent magnetic anisotropy of sputtered $MgO/Co_{40}Fe_{40}B_{20}/Ta$ structures, Appl. Phys. Lett. **96**, 212503 (2010).

[19] T. Nozaki, Y. Shiota, M. Shiraishi, T. Shinjo, and Y. Suzuki, Voltage-induced perpendicular magnetic anisotropy change in magnetic tunnel junctions, Appl. Phys. Lett. **96**, 022506 (2010).

[20] Y. Kato, H. Yoda, Y. Saito, S. Oikawa, K. Fujii, M. Yoshiki, K. Koi, H. Sugiyama, M. Ishikawa, T. Inokuchi, N. Shimomura, M. Shimizu, S. Shirotori, B. Altansargai, Y. Ohsawa, K. Ikegami, A. Tiwari, and A. Kurobe, Giant voltage-controlled magnetic anisotropy effect in a crystallographically strained CoFe system, Appl. Phys. Express **11**, 053007 (2018).

[21] C.-G. Duan, J. P. Velev, R. F. Sabirianov, Z. Zhu, J. Chu, S. S. Jaswal, and E. Y. Tsymbal, Surface Magnetoelectric Effect in Ferromagnetic Metal Films, Phys. Rev. Lett. **101**, 137201 (2008).

[22] M. K. Niranjan, C.-G. Duan, S. S. Jaswal, and E. Y. Tsymbal, Electric field effect on magnetization at the Fe/MgO(001) interface, Appl. Phys. Lett. **96**, 222504 (2010).

[23] J. Zhang, P. V. Lukashev, S. S. Jaswal, and E. Y. Tsymbal, Model of orbital populations for voltage-controlled magnetic anisotropy in transition-metal thin films, Phys. Rev. B **96**, 014435 (2017).

[24] K. Nakamura, R. Shimabukuro, Y. Fujiwara, T. Akiyama, T. Ito, and A. J. Freeman, Giant Modification of the Magnetocrystalline Anisotropy in Transition-Metal Monolayers by an External Electric Field, Phys. Rev. Lett. **102**, 187201 (2009).

[25] K. Nakamura, T. Nomura, A. M. Pradipto, K. Nawa, T. Akiyama, and T. Ito, Effect of heavy-metal insertions at Fe/MgO interfaces on electric-field-induced modification of magnetocrystalline anisotropy, J. Magn. Magn. Mater. **429**, 214 (2017).

[26] S. Kwon, P. V. Ong, Q. Sun, F. Mahfouzi, X. Li, K. L. Wang, Y. Kato, H. Yoda, P. K. Amiri, and N. Kioussis, Colossal electric field control of magnetic anisotropy at ferromagnetic interfaces induced by iridium overlayer, Phys. Rev. B **99**, 064434 (2019).

[27] K. L. Wang, J. G. Alzate, and P. K. Amiri, Low-power non-volatile spintronic memory: STT-RAM and beyond, J. Phys. D: Appl. Phys. **46**, 074003 (2013).

[28] P. E. Blöchl, Projector augmented-wave method, Phys. Rev. B **50**, 17953 (1994).

[29] G. Kresse and J. Furthmüller, Efficient iterative schemes for ab initio total-energy calculations using a plane-wave basis set, Phys. Rev. B **54**, 11169 (1996).

[30] J. P. Perdew, K. Burke, and M. Ernzerhof, Generalized Gradient Approximation Made Simple, Phys. Rev. Lett. **77**, 3865 (1996).

[31] D. D. Koelling and B. N. Harmon, A technique for relativistic spin-polarised calculations, J. Phys. C: Solid State **10**, 3107 (1977).

[32] Ph. Kurz, F. Förster, L. Nordström, G. Bihlmayer, and S. Blügel, Ab initio treatment of noncollinear magnets with the full-potential linearized augmented plane wave method, Phys. Rev. B **69**, 024415 (2004).

[33] D. Odkhuu, S. H. Rhim, N. Park, and S. C. Hong, Extremely large perpendicular magnetic anisotropy of an Fe(001) surface capped by 5*d* transition metal monolayers: A density functional study, Phys. Rev. B **88**, 184405 (2013).

[34] S. Blügel, Two-dimensional Ferromagnetism of 3*d*, 4*d*, and 5*d* Transition Metal Monolayers on Noble Metal (001) Substrates, Phys. Rev. Lett. **68**, 851 (1992).

[35] A. Valdivia, D. J. Tweet, and J. F. Conley, Jr., Atomic layer deposition of two dimensional MoS_2 on 150 mm substrates, J. Vac. Sci. Technol. A **34**, 021515 (2016).

[36] T. Nozaki, A. Koziol-Rachwal, M. Tsujikawa, Y. Shiota, X. Xu, T. Ohkubo, T. Tsukahara, S. Miwa, M. Suzuki, S. Tamaru, H. Kubota, A. Fukushima, K. Hono, M. Shirai, Y. Suzuki, and S. Yuasa, Highly efficient voltage control of spin and enhanced interfacial perpendicular magnetic anisotropy in iridium-doped Fe/MgO magnetic tunnel junctions, NPG Asia Mater. **9**, e451 (2017).

[37] D. Odkhuu and N. Kioussis, Strain-driven electric control of magnetization reversal at multiferroic interfaces, Phys. Rev. B **97**, 094404 (2018).

[38] D.-S. Wang, R. Wu, and A. J. Freeman, First-principles theory of surface magnetocrystalline anisotropy and the diatomic-pair model, Phys. Rev. B **47**, 14932 (1993).